JACS
JOURNAL OF THE AMERICAN CHEMICAL SOCIETY

Article

pubs.acs.org/JACS

Three-Dimensional Imaging of Transparent Tissues via Metal Nanoparticle Labeling

Abdullah Muhammad Syed,[†,#] Shrey Sindhwani,[†,#] Stefan Wilhelm,[†] Benjamin R. Kingston,[†] Dennis S. W. Lee,[‡] Jennifer L. Gommerman,[‡] and Warren C. W. Chan*[,†,§,∥,⊥]

[†]Institute of Biomaterials and Biomedical Engineering, University of Toronto, Rosebrugh Building, Room 407, 164 College Street, Toronto, Ontario M5S 3G9, Canada

[‡]Department of Immunology, University of Toronto, Medical Sciences Building, 1 King's College Circle, Toronto, Ontario M5S 1A8, Canada

[§]Terrence Donnelly Centre for Cellular and Biomolecular Research, University of Toronto, Room 230, 160 College Street, Toronto, Ontario M5S 3E1, Canada

[∥]Department of Chemical Engineering, University of Toronto, 200 College Street, Toronto, Ontario M5S 3E5, Canada

[⊥]Department of Material Science and Engineering, University of Toronto, Room 450, 160 College Street, Toronto, Ontario M5S 3E1, Canada

Supporting Information

ABSTRACT: Chemical probes are key components of the bioimaging toolbox, as they label biomolecules in cells and tissues. The new challenge in bioimaging is to design chemical probes for three-dimensional (3D) tissue imaging. In this work, we discovered that light scattering of metal nanoparticles can provide 3D imaging contrast in intact and transparent tissues. The nanoparticles can act as a template for the chemical growth of a metal layer to further enhance the scattering signal. The use of chemically grown nanoparticles in whole tissues can amplify the scattering to produce a 1.4 million-fold greater photon yield than obtained using common fluorophores. These probes are non-photobleaching and can be used alongside fluorophores without interference. We demonstrated three distinct biomedical applications: (a) molecular imaging of blood vessels, (b) tracking of nanodrug carriers in tumors, and (c) mapping of lesions and immune cells in a multiple sclerosis mouse model. Our strategy establishes a distinct yet complementary set of imaging probes for understanding disease mechanisms in three dimensions.

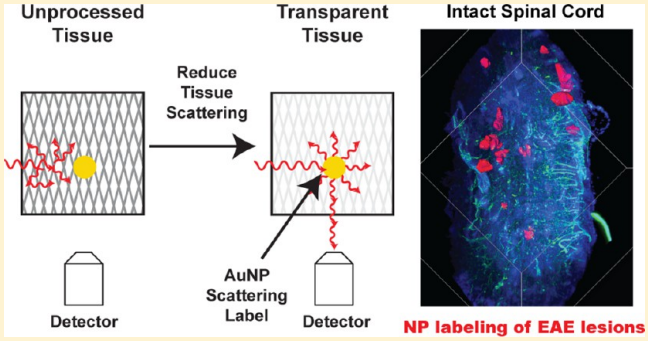

INTRODUCTION

Advances in chemical probe design and microscopy have enabled the elucidation of many disease processes. Small organic molecules, fluorescent proteins, and nanoparticle probes have been chemically designed to target specific receptors on cells and tissues. These probes are then imaged using optical microscopy to visualize the spatial context of disease mechanisms.[1] These probes are well-characterized with respect to bioconjugation and optical properties for two-dimensional (2D) imaging of cells and tissues.[2,3] Recently, there has been a focus on three-dimensional (3D) tissue imaging, which allows cells and biomolecules to be imaged within their intact biological contexts.[4−8] This can be achieved by making tissues optically transparent, which allows light to penetrate into and out of them. 3D imaging is providing new insights into large-scale biological questions, such as neuronal wiring of mammalian brains and mechanisms of development in human embryos.[9] To ensure that optical clearing becomes an important tool for broad research use, there is a need to develop new chemical probes and staining techniques for 3D imaging of optically transparent tissues. However, comprehensive evaluation and improvements in the chemical design of optical probes for 3D tissue imaging have not kept pace with parallel advances in techniques that make tissues transparent.

Small organic fluorescent molecules conjugated to antibodies and fluorescent proteins genetically incorporated into cells are the predominant methods for labeling of optically transparent tissues for 3D imaging, but these molecules suffer from autofluorescence, photobleaching, and weak signal.[10] Other imaging approaches based on photoacoustic tomography and Raman scattering either cannot provide cellular resolution or suffer from low acquisition speed.[11] Nanoparticle-based probes can overcome a number of limitations of both small organic molecules and fluorescent proteins because they have been demonstrated to produce large extinction coefficients.[12] The

Received: April 20, 2017
Published: June 22, 2017

DOI: 10.1021/jacs.7b04022
J. Am. Chem. Soc. 2017, 139, 9961−9971

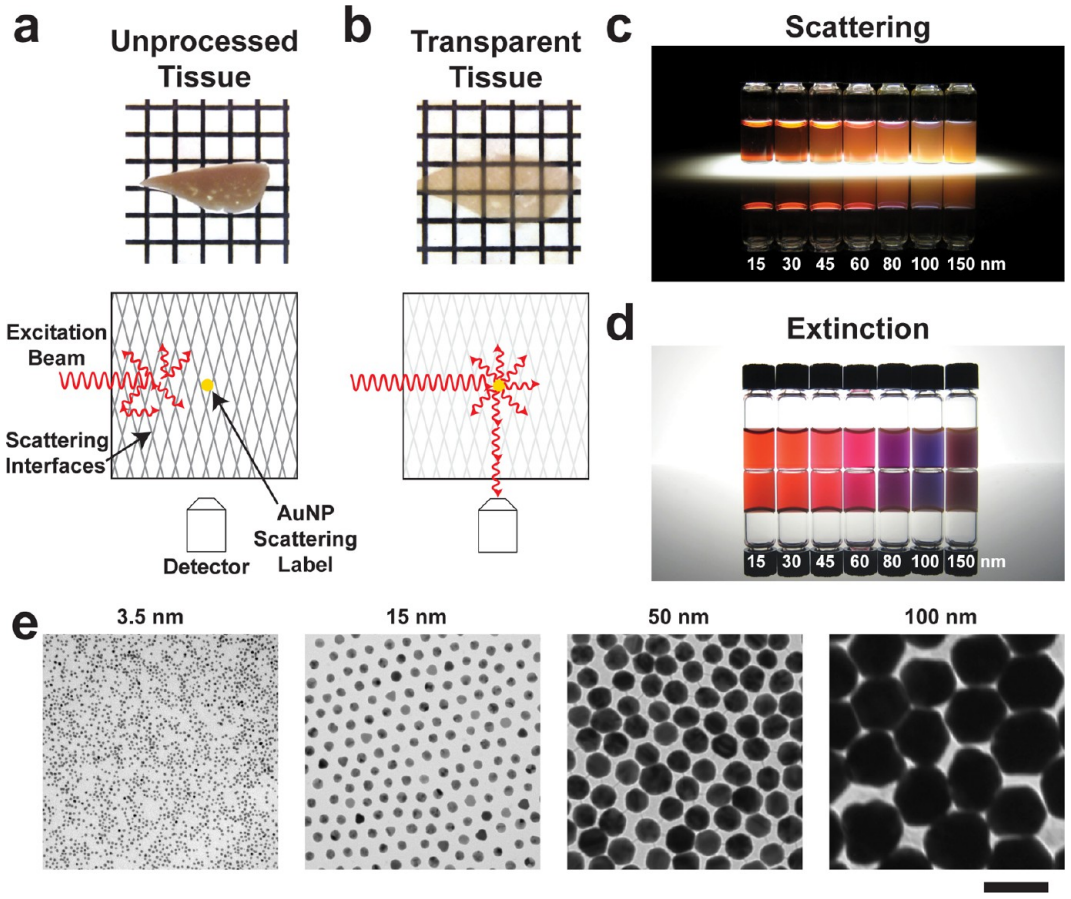

Figure 1. Scattering of metal nanoparticles provides contrast for 3D imaging of intact tissues. (a) In model tissues (1 mm mouse liver sections), light is scattered by lipid−aqueous interfaces, limiting its penetration depth. (b) Rendering intact tissues transparent using tissue-clearing techniques suppresses intrinsic scattering and allows light to penetrate into the tissue. This light can then be scattered by gold nanoparticle (AuNP) labels and collected by a detector placed at an angle from the excitation source. (c, d) Photographs of (c) epi- and (d) trans-illuminated vials of a series of AuNPs with varying diameters. This provides a visual display of their size-dependent scattering and extinction spectra. AuNPs have size-dependent scattering yields and molar extinction coefficients over a wide diameter range of 1−200 nm. (e) Examples of AuNPs that were synthesized with diameters of 3−100 nm. Transmission electron microscopy analysis confirms narrow nanoparticle size distribution. The scale bar indicates 100 nm.

scattering properties of these probes have been used extensively in 2D histology sections and *in vitro* cultures.[13−15] However, optical scattering has not been explored for 3D optical imaging. Previously, we investigated the distribution of nanoparticles using 3D fluorescence imaging of intact but optically cleared tissues.[16,17] On the basis of these observations, we set out to investigate the application of nanoparticle-based optical scattering probes to label features in tissues for 3D imaging. Here, we show that nanoparticle-based scattering contrast agents can serve as an alternative to fluorescence for detecting low-abundance targets in intact transparent tissues. Additionally, by chemically reducing gold or silver onto nanoparticles we can increase the scattering of nanoparticles to amplify the signal and allow for ultrasensitive detection of specific tissue structures.

RESULTS

A fundamental principle in making tissues optically transparent is to reduce intrinsic scattering of tissues[18−21] by removing light scattering components and matching the refractive index in the remaining tissue.[4−8] This allows light to penetrate deep into tissues, which enables 3D microscopic imaging of intact tissues. We rationalized that because the clearing processes reduce intrinsic scattering of the tissue, probes that generate scattering signal will provide contrast within these tissues (Figure 1a,b). The signal-to-noise ratio for these scattering probes will then be determined by the amount of clearing and the scattering coefficient of the probe. Specifically, a nanoparticle scattering label, such as a gold nanoparticle (AuNP), placed within this tissue scatters any excitation light in all directions (Figure 1b). This scattering is then visualized by placing the detector or camera at an angle from the source of illumination (Figure 1b). To visualize the scattering from model probes, we synthesized AuNPs with diameters in the range of 15−150 nm and found that they scatter and absorb light efficiently with size-dependent spectra (Figures 1c,d and S1).[22,23] The synthesis of 3.5-nm AuNPs was performed using tannic acid reduction. The synthesis of AuNPs with diameters greater than 30 nm requires 15-nm AuNPs as seeds, which themselves are prepared by citrate reduction of chloroauric acid. These seeds can be further grown to yield nanoparticles with diameters between 30 and 200 nm through further hydroquinone-mediated reduction at room temperature. This yields nanoparticles with controllable size and narrow size distribution (Figure 1e). The principle of scattering-based contrast applies to all nanoparticle compositions, including silver, silica, and polystyrene, but is particularly pronounced for silver and gold because they possess low refractive indices compared with cleared tissues (Table S1).

DOI: 10.1021/jacs.7b04022
J. Am. Chem. Soc. 2017, 139, 9961−9971

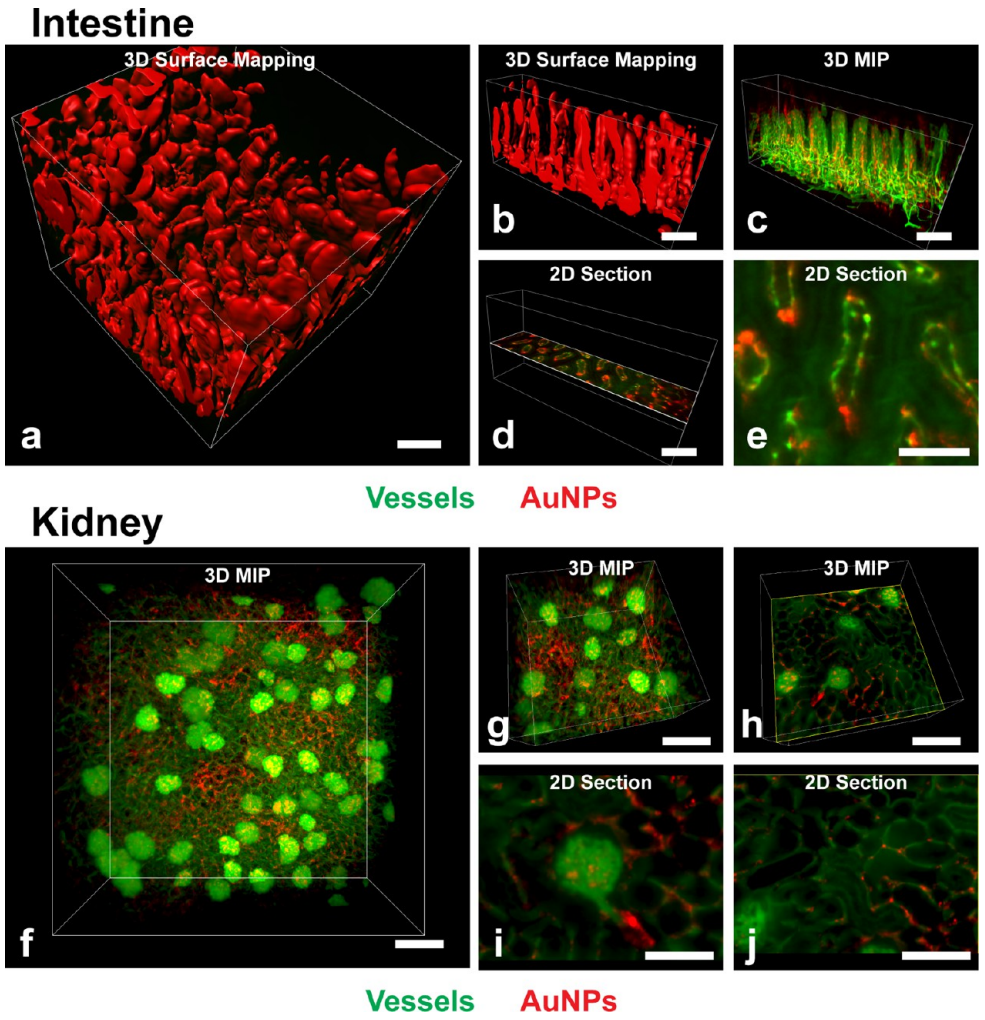

Figure 2. Gold nanoparticle (AuNP) scattering signal visualized in mouse intestine and kidney tissues using 3D dark-field microscopy. (a) Surface mapping of the 3D image of intestinal tissue containing 50-nm AuNPs, showing the morphology of villi. (b) Smaller segment of the image from (a). (c) 3D maximum intensity projection (MIP) of the same region of intestinal tissue showing the arrangement of blood vessels and distribution of AuNPs. (d) Position of the 2D section in (e) showing the distribution of AuNPs within a single villus. (f, g) 3D maximum intensity projection of blood vessels and AuNPs within kidney tissue with brightly stained glomeruli visible. (h) Location of 2D sections of (i) and (j) showing the local distribution of AuNPs within and around a glomerulus. Scale bars indicate 200 μm for (a), (b), (c), (d), (f), (g), and (h) and 100 μm for (e), (i), and (j).

Metal Nanoparticle Scattering Can Be Visualized in Cleared Tissues. We first determined whether the scattering signal could be detected in 3D in model mouse tissues. We intravenously injected 2×10^{12} AuNPs (core size of 50 nm, 100 mg/kg) into CD1-nude mice, sacrificed them 24 h post-injection, and cleared the organs using protocols reported previously.[16,17] The resulting tissues were transparent with a slight red coloration due to the extinction profile of AuNPs. After matching of the refractive index using 67% (v/v) aqueous solution of 2′2-thiodiethanol (TDE), we placed the cleared tissue in a Zeiss Lightsheet Z.1. microscopy system with the emission filters removed to detect the scattering signal in a method known as dark-field microscopy.[24,25] We found that we could visualize nanoparticle scattering using this approach in mouse livers (Figure S2), intestines (Figure 2a–e, Video S2), and kidneys (Figure 2f–j, Video S1) and that both scattering and fluorescence signals could be detected for more than 1 mm in imaging depth. The imaging depth is theoretically unlimited if sufficient tissue transparency is achieved. In a transparent polydimethylsiloxane block, single 100-nm AuNPs could be imaged to depths of up to 3.3 mm (Figure S3). We also attempted to image fluorescence and scattering using the same excitation wavelength and found that the signals could be separated using a standard emission filter because of their distinct emission profiles (Figure S4).

Nanoparticle Scattering Produces Ideal Optical Properties for Ultrasensitive Imaging. To assess the optical performance of noble-metal nanoparticles for 3D imaging, we then characterized the optical contrast generated by elastic scattering of single gold or silver nanoparticles compared with the photoluminescence of single fluorescent molecules. We calculated the optical properties of gold and silver nanoparticles according to Mie theory on the basis of previously measured optical constants.[26] We found that 50-nm AuNPs possess a molar extinction coefficient of 2.1×10^9 M^{-1} cm^{-1} (Figure 3a,b). This molar extinction coefficient is ~8000-fold greater than those of typical organic fluorophores (Alexa Fluor 647, eosin) and fluorescent proteins (green fluorescent protein) (Figure 3a,b). This increased extinction coefficient means that fewer probes are required to generate equivalent

DOI: 10.1021/jacs.7b04022
J. Am. Chem. Soc. 2017, 139, 9961–9971

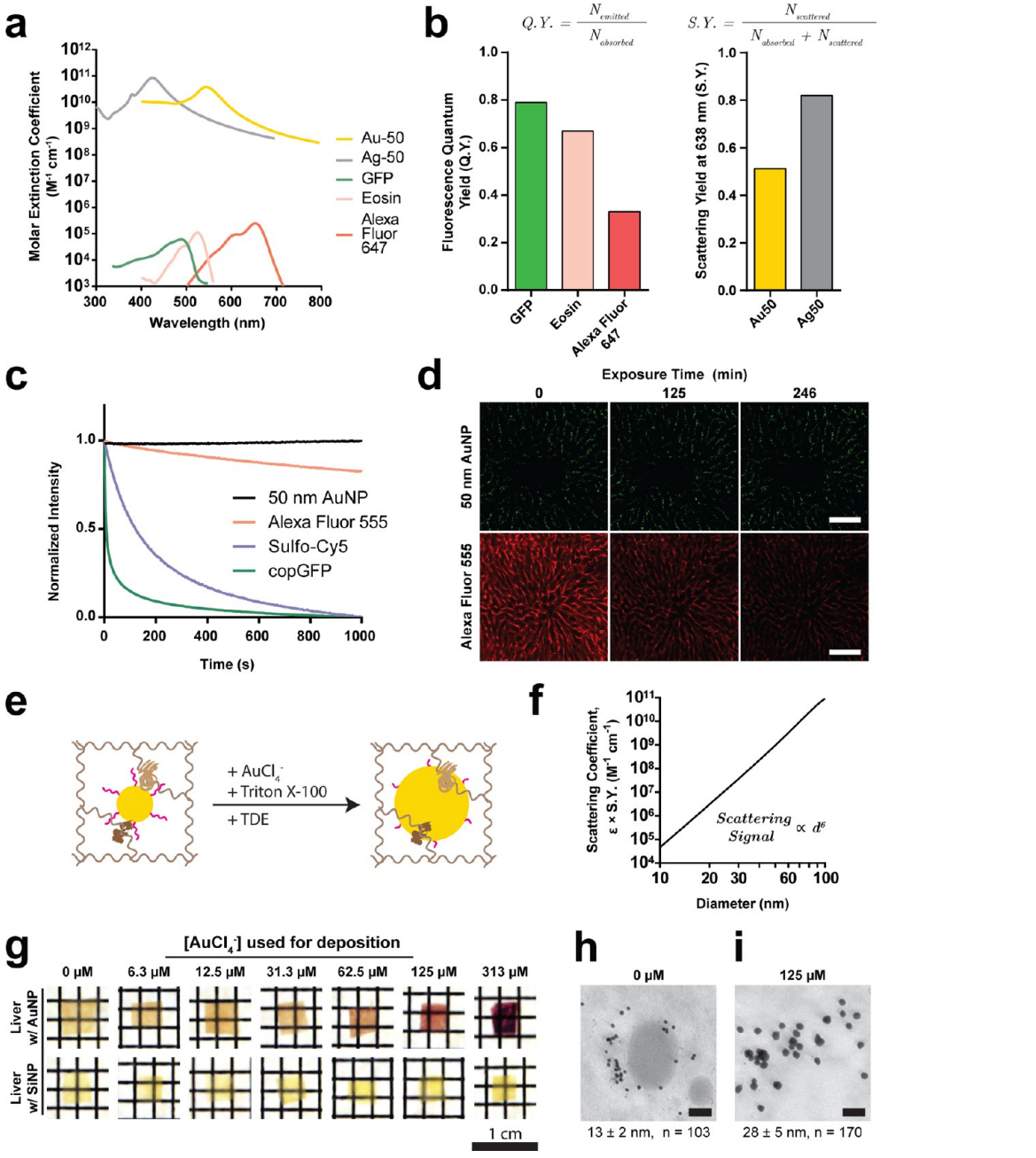

Figure 3. Nanoparticle scattering signals do not photobleach and can be amplified a million-fold in whole tissues. (a) The molar extinction coefficients of 50-nm silver and gold nanoparticles (AgNPs and AuNPs respectively) are orders of magnitude higher than those of typical chromophores and fluorophores while (b) the photon yield of scattering (S.Y.) is similar to the fluorescence quantum yield (Q.Y.). (c) The scattering signal of AuNPs does not photobleach compared with the signals of common fluorophores (Alexa Fluor 555, Sulfo-Cy5, and copGFP). (d) When a dual blood vessel labeling strategy was used in mouse liver, AuNPs did not show any change in scattering intensity over this period while the Alexa Fluor 555 signal diminished as a result of photobleaching. (e) The scattering signal can be further amplified through *in situ* deposition of free $AuCl_4^-$ onto AuNPs using seed-mediated electroless deposition in the presence of a mild reducing agent (Triton X-100). (f) Mie theory predictions of scattering coefficients of AuNPs ranging in diameter (d) from 10 to 100 nm. Mie theory predicts that an increase in AuNP diameter from 10 nm to 100 nm results in 1.2 million-fold increase (approximately proportional to d^6) of the scattering coefficient (which is proportional to the brightness of the scattering signal). (g) Liver tissues with 13-nm AuNPs or 50-nm SiNPs incubated with varying concentrations of $AuCl_4^-$ show that the size of the resulting AuNPs is controllable and specific. (h, i) Representative transmission electron microscopy images show the increased size and consistent morphology of the amplified AuNPs. Scale bars indicate (d) 100 μm and (h, i) 100 nm.

signal. Next, we compared the quantum yield of fluorophores to the scattering yield of nanoparticles, which are both measures of the efficiencies with which excitation photons are converted into emitted photons. The quantum yield of fluorophores typically varies between 10% and 80%, which is comparable to the scattering yield of 51% at 638 nm for 50-nm AuNPs (Figure 3b). The brightness of the imaging signal is proportional to the product of the molar extinction coefficient and the quantum yield or scattering yield. Since the yields of scattering and fluorescent agents are similar while the molar extinction coefficient is higher for the former, the expected output signal for a 50-nm AuNP would be 13000-fold larger than that

DOI: 10.1021/jacs.7b04022
J. Am. Chem. Soc. 2017, 139, 9961−9971

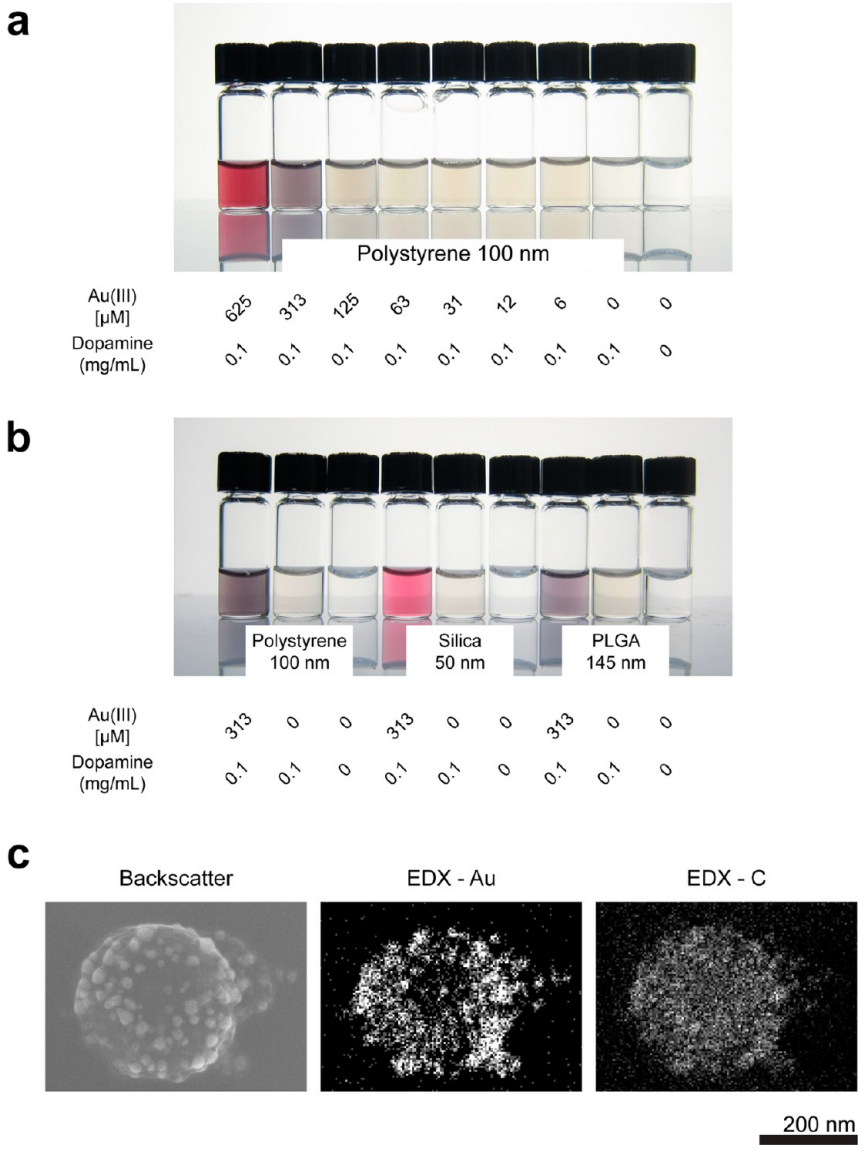

Figure 4. A generalized dopamine-based strategy for gold deposition on different materials expands dark-field imaging for studying material−tissue interactions. (a) Incubation of 100-nm polystyrene beads with dopamine followed by subsequent incubation in $AuCl_4^-$ solution yields a change in solution color. The initial dopamine coating on the beads yields a black color that changes from light brown to purple to red in a concentration-dependent manner as a result of deposition of gold nanoparticles on the surface. (b) This strategy yielded similar results on other materials such as silica and PLGA nanoparticles with the appearance of red (silica) and purple (PLGA) color after incubation with Au(III) solution. (c) Gold deposition was confirmed by scanning electron microscopy coupled with energy-dispersive X-ray spectroscopy (EDX) analysis of gold and carbon on polystyrene nanoparticles. Gold (EDX - Au,Lα_1) was observed from confined spots on the shell, which showed deposition of small AuNPs, whereas a homogeneous carbon signal (EDX - C,K$\alpha_{1,2}$) could be detected from the core, which reflects the presence of organic compounds, such as polystyrene.

expected from Alexa Fluor 647. Interestingly, the signal is even greater if AuNPs larger than 50 nm are used because there is a size-dependent relationship between particle size, molar extinction coefficient, and scattering yield (Figure S5). For example, a 200-nm AuNP has an extinction coefficient of 1.2×10^{11} M^{-1} cm^{-1} and a scattering yield of 88%, which would increase the signal another 98-fold compared with a 50-nm AuNP (Figure S5). This scattering contrast is sufficient to enable a single 100-nm AuNP to be detected using dark-field microscopy (Figure S3). Another potential scattering material is silver, which has even more efficient scattering and a blue-shifted spectrum (Figure 3a). A 50-nm silver nanoparticle (AgNPs) has a molar extinction coefficient of 7.1×10^8 M^{-1} cm^{-1} with a scattering efficiency of 82% at a wavelength of 638 nm (Figure 3a,b). In addition to noble metals, organic nanoparticles can be chemically modified to produce a scattering signal by the deposition and growth of a noble-metal layer on their surface.[27] Figure 4 shows the growth of a gold layer on the surfaces of dopamine coated silica, polystyrene, and poly(lactide-*co*-glycolide) (PLGA) nanoparticles to amplify their scattering properties.

Next, we assessed the photostability of AuNP scattering probes in comparison with model fluorophores. Photostability is an important parameter when comparing optical probes because it quantifies the stability of the observed signal over time under constant excitation. Probes that are photostable enable long-term analysis of molecules and cells, which provides improved reproducibility of the optical signal over

DOI: 10.1021/jacs.7b04022
J. Am. Chem. Soc. 2017, 139, 9961−9971

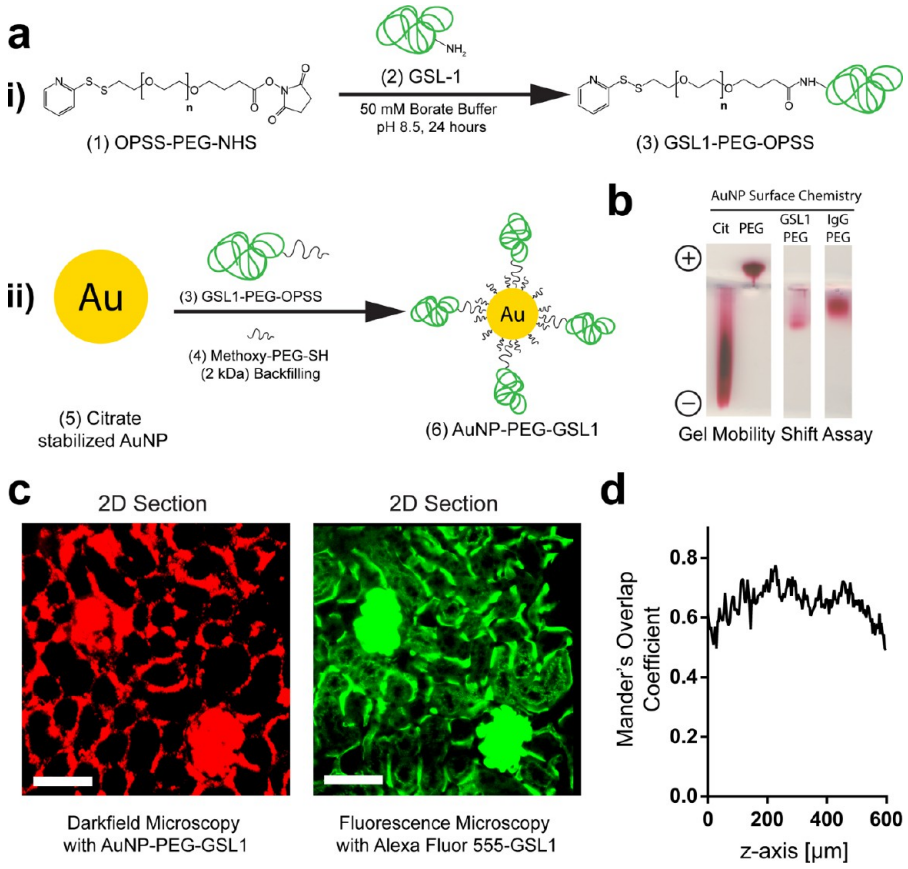

Figure 5. Molecular labeling of mouse kidneys for mapping vasculature using nanoparticle scattering agents. (a) AuNPs are surface-modified with GSL-1 using a heterobifunctional linker, OPSS-PEG-NHS. (b) Gel mobility shift assay confirms surface modification. (c) 2D sections taken from a 3D image of mouse kidney tissue showing GSL-1-modified AuNPs visualized with dark-field microscopy and Alexa Fluor 555-modified GSL-1 visualized using fluorescence lightsheet microscopy, showing overlap between the two labels. (d) Mander's coefficient as a function of depth shows that AuNP-GSL1 consistently colocalizes with the free fluorescently labeled molecule. Scale bars represent 100 μm. GSL-1: *Griffonia simplificolia* lectin I.

multiple measurements. We compared the photostability of 100-nm AuNPs with copGFP, Cy5, and Alexa Fluor 555 by continuous excitation of these probes in the same cleared tissues. Using a lightsheet microscope configured for dark-field imaging and a laser power density of ~20 W/cm^2, we found that the half-life of copGFP (18.9 W/cm^2) was 7 s, compared with 118 s for Cy5 (12.4 W/cm^2) and 3218 s for Alexa Fluor 555 (28.1 W/cm^2) (Figure 3c). We observed that the scattering intensity of tissues stained with AuNPs did not decrease in comparison to Alexa Fluor 555-labeled tissues (Figure 3c,d). After 1000 s of imaging, the normalized signal from AuNPs (12.4 W/cm^2) was over 100-fold higher than those from copGFP and Cy5 and 18% higher than that from Alexa Fluor 555 (Figure 3c). These observations are consistent with the theoretical explanations of scattering. Fluorophores photobleach because light degrades their molecular structure. In contrast, AuNPs are not susceptible to photo-oxidation, and hence, their signal is maintained throughout the excitation of the tissue samples.[28,29]

Nanoparticles Can Be Grown within Cleared Tissues To Amplify the Scattering Signal. As a final step of characterization, we explored whether nanoparticle scattering signals could be amplified for the detection of rare targets in tissues. The scattering coefficient is proportional to d^6 for AuNPs with diameters (d) between 1 and 100 nm, so we asked whether we could grow the AuNPs after attachment to tissue structures (Figure 3e,f). By increasing the size of a tissue-tagged AuNP from 10 to 100 nm in diameter, we expect to observe a 2 million-fold increase in scattering (Figure 3f). In solution, the size of AuNPs can be increased by reacting small nanoparticles with Au(III) ions and reducing agents, but the AuNPs have to be grown with a consistent and uniform distribution in the tissues in order to obtain consistent signals.[23] A challenge of growing larger nanoparticles in whole tissues is that the chemical reagents have to diffuse throughout the tissue, and any fast-acting reducing agents would create inhomogeneous amplification and bias the interpretation of the images. We examined a series of reducing agents (1,4-benzenediol, trisodium citrate, and Triton X-100) and found that Triton X-100 reacts slow enough to enable uniform nanoparticle growth throughout the cleared tissue. We preincubated 1 mm mouse liver tissue slices for 1 day each in solutions of 0.1% Triton X-100, Au(III) ions, and 67% 2,2′-thiodiethanol (TDE) for refractive index matching. The tissues changed color to become more red up to a concentration of 125 μM and black at the highest concentration of 313 μM (Figure 3g). This gold deposition was uniform with no noticeable gradient in concentration across the tissue (Figure 3g). We then examined these tissues using transmission electron microscopy and found that AuNPs with a diameter of 13 ± 2 nm in liver tissue grew to a final size of 28 ± 5 nm when incubated with 125 μM Au(III) (Figures 3h,i and S6). According to Mie theory, this

DOI: 10.1021/jacs.7b04022
J. Am. Chem. Soc. 2017, 139, 9961−9971

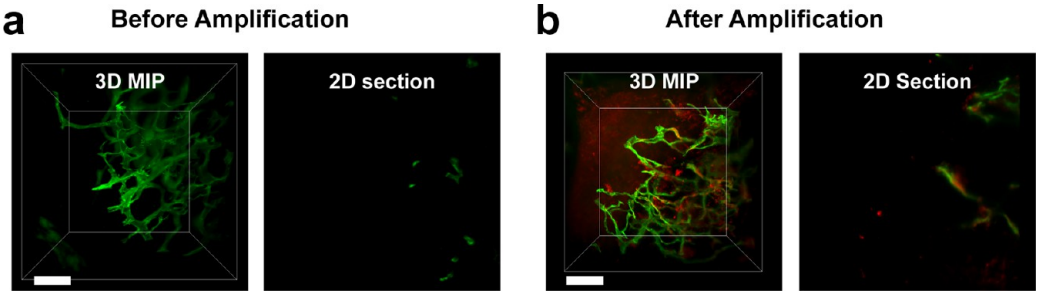

Figure 6. *In situ* deposition of Au(III) enables the detection of low-accumulation AuNPs. MDA-MB-435 xenograft tumors labeled with GSL-1 for blood vessels (green) and AuNP scattering (red). (a) 15-nm AuNPs could not be detected in the original tissue because of the combination of low accumulation and weak scattering yield. (b) *In situ* deposition of Au(III) using 125 μM $AuCl_4^-$ with the addition of the reducing agent Triton X-100 resulted in a detectable signal throughout the tissue, including near the blood vessel surface and diffuse regions away from the vessels. The two 3D images were collected using identical imaging conditions on the same day. Scale bars indicate 200 μm. MIP: maximum-intensity projection.

corresponds to an 86-fold increase in the scattering coefficient (Figure 3f–i). The staining appeared to be specific since nanoparticles were not observed in a negative control tissue containing silica nanoparticles that was treated with the same solutions of Au(III) and Triton X-100 (Figure 3g, S6). This enhancement can also be achieved using Ag(I) ions, which offers extra possibilities for tissue staining because Ag(I) can be nucleated by many proteins to allow mapping of the protein content over whole tissues.[30] This combination of strong optical contrast, high photostability, and simple *in situ* signal amplification presents a distinct advantage of scattering labels over fluorophores for labeling and imaging 3D tissues.

To show the generality of 3D dark-field microscopy using nanoparticle scattering probes, we demonstrate three specific applications: (a) targeted scattering probes for molecular imaging of intact tissues, (b) visualization of nanoparticle transport and accumulation in mouse tumor models, and (c) characterization of lesions in a mouse model of multiple sclerosis. Beyond our demonstrated applications, we envision that these techniques can be applied to all types of applications that require ultrasensitive staining of tissue structures or for analyzing a larger number of probes.

Molecular Labeling of Cleared Tissues Can Be Achieved by Conjugating Proteins to the Nanoparticle Surface. First, we demonstrate the ability to use AuNP scattering probes for molecular analysis. We developed a conjugation strategy for synthesizing vascular-targeting AuNPs by reacting AuNPs with a lectin that has specific affinity for mouse blood vessels.[31] We first covalently conjugated fluorescent *Griffonia simplicifolia* lectin I (Cy5) to a heterobifunctional 5000 Da poly(ethylene glycol) (*o*-pyridyl disulfide poly(ethylene glycol) succinimidyl ester, OPSS-PEG-NHS) (Figure 5a).[32,33] The OPSS group was then reacted with citrate-stabilized AuNPs to form GSL-1-conjugated AuNP probes (Figure 5a). We verified the conjugation of GSL-1 onto the surface of AuNPs using a gel mobility shift assay and SDS-PAGE (Figures 5b and S7). The fluorescence from the Alexa Fluor 555 labeling of the conjugate colocalizes with the AuNP location on the gel, reflecting the stability of the conjugation chemistry (Figure S7c). We next tested these vascular-targeting probes *in vivo* by injecting them intravenously into a CD-1 nude mouse and allowing them to circulate for 2 h, with Alexa Fluor 555-conjugated free GSL-1 injected in the same animal as a positive control. We visualized kidney vasculature from the same sample using dark-field and fluorescence microscopy and found colocalization between the two probes (Figure 5c). Quantification of the Mander's coefficient between the two probes revealed approximately 60% overlap throughout the 0.6 mm stack (Figure 5d). This probe design and conjugation strategy provides a simple means of synthesizing AuNP-based molecular labels for use in 3D tissue imaging.

***In Situ* Amplification Allows the Visualization of Rare Nanoparticles in Tumors.** Next, we demonstrate the ability to visualize hard-to-detect AuNPs in tumors. Currently, nanoparticle delivery systems are expected to improve the treatment and detection of cancer, but recent studies show low nanoparticle accumulation in tumors.[34] This has led to a major focus on studying, optimizing, and characterizing the delivery of nanoparticles into tumors. However, the low amount of nanoparticles accumulating in the tumor makes it challenging to visualize their distribution with respect to vasculature and stromal cells. This problem is particularly relevant for smaller nanoparticles, which have improved toxicity profiles but lower accumulation and lower signals in most imaging modalities. We investigated whether 15-nm AuNPs could be visualized in an MDA-MB-435 xenograft mouse tumor model using our *in situ* growth strategy. In cleared tumor tissues without gold deposition, we found that the AuNP signal could not be visualized because of the low accumulation of AuNPs in this model (Figure 6a, Video S3). Following *in situ* growth with 125 μM Au(III), we were able to visualize both diffuse and localized signals from AuNPs (Figure 6b, Video S4), as designated by the red signals throughout the image. These results demonstrate a simple and powerful strategy for examining the distribution of nanocarriers in 3D tumor tissues, and the outcomes of these fundamental studies could result in the improved design of therapeutic nanoparticles for cancer treatment.

Nanoparticle Formation in Intact Spinal Cords Allows Visualization of Lesions in a Mouse Model of Multiple Sclerosis. The last application we demonstrate with our technique is the mapping of demyelinated lesions in a mouse model of multiple sclerosis (MS) with respect to inflammatory cells (experimental autoimmune encephalomyelitis, EAE). Conventionally, the analysis of these lesions is performed using 2D histology techniques with chromogenic staining or by flow cytometry.[35,36] These methods cannot capture the full 3D volume of lesions or the relationship between these structures and inflammatory cell types because they either take a small fraction of the tissue (histology) or destroy the architecture to analyze cells (flow cytometry).[37] Our approach of 3D imaging generates images equivalent to 600 to 800 histology slices while preserving the relationships between multiple fluorescence and scattering channels and is significantly less labor-intensive. We

DOI: 10.1021/jacs.7b04022
J. Am. Chem. Soc. 2017, 139, 9961–9971

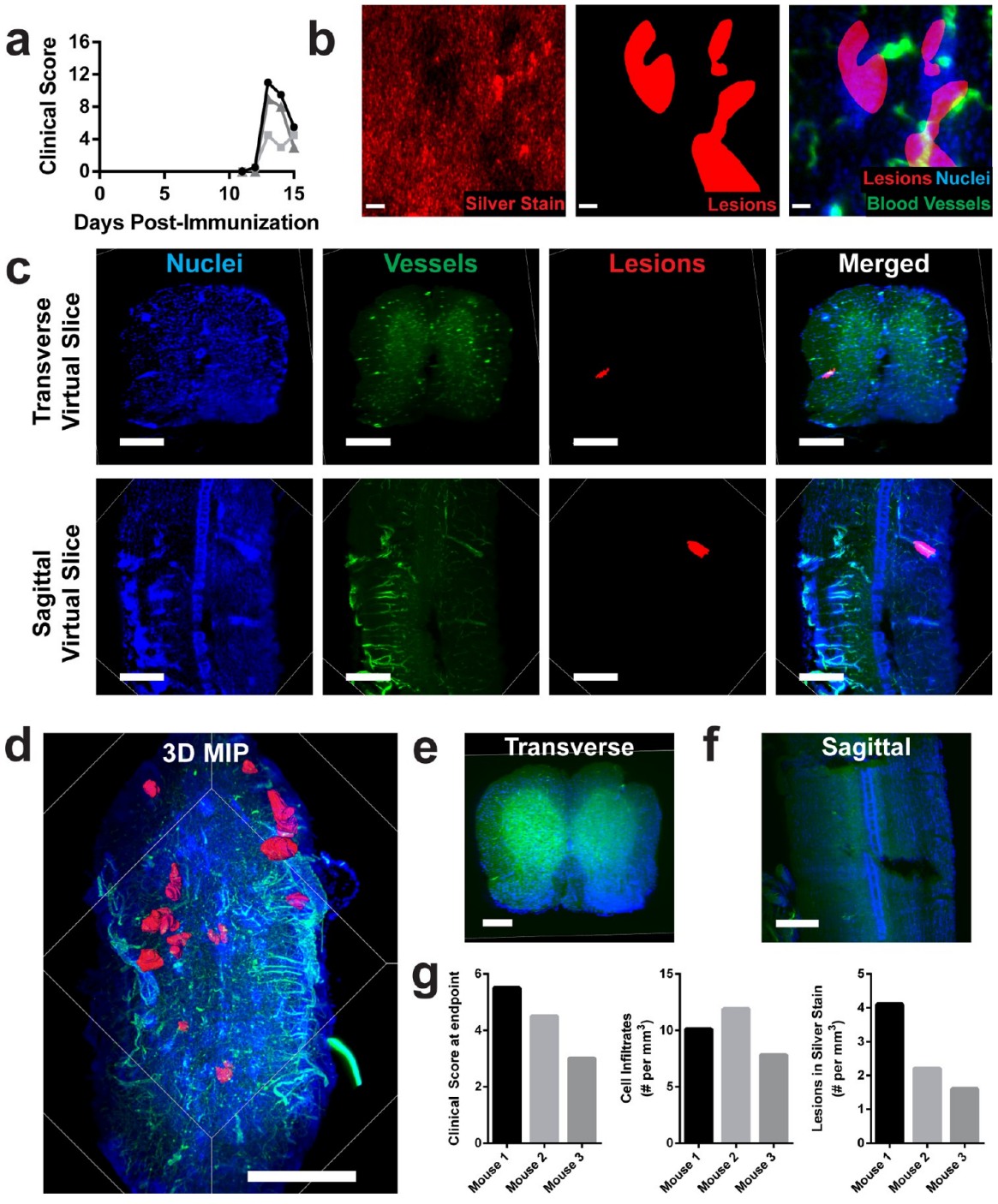

Figure 7. Multispectral structural analysis of an experimental autoimmune encephalomyelitis (EAE) model. (a) Clinical profile of three SJL/J mice with EAE measured on a 16-point scale with expected clinical profile. Spinal cords were extracted from these mice at 15 days postimmunization, fixed, cleared, and stained for lesions using silver deposition, for nuclei using DAPI, and for blood vessels using GSL1-A555. (b) 2D virtual slice of lesions within the spinal cord, visible as dark regions in the silver-stained image, were manually segmented to generate a binary image of the lesions. This is shown by overlaying with corresponding blood vessels and nuclei. (c) Transverse and sagittal sections of the entire spinal cord shown in the DAPI, GSL1, and lesion channels. Cell infiltrates, dilated blood vessels, and corresponding lesions are seen in context, showing the partial colocalization of these features. Cell infiltration closely follows unusual and enlarged blood vessels, but only some of these areas have demyelination. (d) 3D maximum intensity projection of a 3.6 mm length of spinal cord showing the relative arrangement of blood vessels, cell infiltrates, and lesions across the whole spinal cord. (e) Transverse and (f) sagittal sections of an unimmunized mouse show a normal distribution of nuclei and lower abundance of dilated blood vessels. (g) End point clinical scores, concentration of cell infiltrates, and lesions shown for each of the three mice characterized. On average only about 28% of cell infiltrates had detectable lesions in the silver stain. Scale bars indicate (b) 20 μm, (c) 450 μm, (d) 1000 μm, (e) 450 μm, and (f) 450 μm. MIP: maximum-intensity projection.

induced EAE by immunizing three female SJL/J mice with 100 μg of $PLP_{139-151}$ injected subcutaneously in the back. These mice were monitored daily for clinical symptoms, such as paralysis, and exhibited peak disease at 12 days postimmunization (Figure 7a). At 15 days postimmunization, we sacrificed the mice and dissected and cleared the intact spinal cords using

DOI: 10.1021/jacs.7b04022
J. Am. Chem. Soc. 2017, 139, 9961−9971

previously established procedures.[16] After clearing the tissues, we incubated them sequentially in 0.1% Triton X-100, deionized water, 10% silver nitrate, and 4% SDS solution to develop silver nanoparticles (AgNPs) throughout the tissue. Our amplification strategy labels myelinated regions because Ag(I) has an affinity for positively charged proteins and the reduction of Ag(I) into nanoparticles yields scattering contrast that allows lesions to be visualized as dark areas within the dark-field channel (Figure 7b, Video S6). It should be noted that this staining strategy is able to label myelin because myelin has a comparatively higher affinity for silver ions than other proteins and that this method will label other argyrophilic proteins in other tissues. We visualized cell infiltrates using 4′,6-diamidino-2-phenylindole (DAPI) and blood vessels using GSL1-A555, and combined with AgNP scattering, we observed nuclei and blood vessels with imaging depths sufficient to visualize the entire 3 mm width of the spinal cord (Figure 7c,d, Video S6). By means of these multichannel 3D images of lesions, it is now possible to examine the structural and cellular aspects of EAE. We observed ∼100 regions of cellular infiltration in a single 3D field of view (2.5 mm × 2.5 mm × 3 mm) within each spinal cord and large numbers of dilated blood vessels and lesions. Interestingly, both cell infiltration and demyelination form around blood vessels and trace along these vessels over distances of up to 500 μm (Figure 7c−e, Video S6). These vessels are particularly enlarged and possess irregular staining patterns compared with nearby vessels without cell infiltration (Table S3). Lesions were not found in unimmunized control mice that served as controls for the EAE model (Figure 7e,f, Video S5). We examined the relationship between lesions and cell infiltrates and found that only 20−40% of cell infiltrates corresponded to lesions, perhaps as a result of a temporal disconnect between leukocyte infiltration and lesion formation (Figure 7g). These studies demonstrate that our amplification strategy in combination with fluorescence labeling enables a 3D analysis of EAE in mouse tissues. This makes it possible for researchers to determine relationships between enlarged vessels, cell infiltrations, and demyelination in future studies, which might lead to improved therapies for MS patients.

DISCUSSION

An important consideration for 3D imaging of intact tissues is the selection of a suitable chemical probe. Chemical probes provide optical contrast and enable one to visualize specific biological molecules in intact tissues. To date, fluorescent proteins and small-molecule dyes have been the only chemical probes investigated for use in 3D optical imaging. In this study, we developed optical scattering probes that enable imaging of intact biological samples using 3D optical microscopy with unprecedented sensitivity. An interesting observation is that the controlled reduction of Au(III) ions onto the surface of the scattering probe leads to significantly enhanced optical scattering, which produces up to a 1.4 million-fold higher optical signal than with fluorophores. This enhanced signal enabled us to visualize nanoparticles in tumors and lesions in the spinal cord of animals with EAE, which would not have been possible without utilizing the unique properties of scattering agents. Furthermore, the scattering probes do not photobleach and have extinction coefficients and photon yields that are orders of magnitude greater than those of organic fluorophores.

In addition to these applications, we envision that this approach will be useful for the detection of faint molecular markers that are stained using antibodies conjugated to small nanoparticles, which are then amplified into larger nanoparticles using gold or silver deposition. Combined with cleared tissues and 3D dark-field microscopy, this would enable single-molecule sensitivity throughout whole mouse organs. For example, gold nanoparticle antibody probes used for electron microscopy could now be visualized in 3D using dark-field microscopy post-amplification. This would allow researchers to perform correlative electron and optical microscopy from the same tissue. Metallic probes such as gold AuNPs have also been used beyond dark-field microscopy because of their photoacoustic and inelastic scattering properties.[38−40] Our technique could be combined to obtain correlative live and *ex vivo* imaging data by photoacoustic tomography and surface-enhanced Raman scattering (SERS) using a single set of metallic probes.

Two main challenges remain with using *in situ* growth as a means for 3D microscopy of rare biomarkers: (1) nonspecific binding and deposition on certain proteins with natural affinities for metal ions; and (2) developing spectrally distinct scattering labels that can used for multiplex analysis due to the uniform rate of metal deposition on nanoparticles. Nonspecific binding and amplification do not have simple solutions. Typically, gold is less likely to result in nonspecific staining compared with silver. Optimized selection of the scattering probe may lead to more specific seed-mediated staining. Another approach is to optimize the incubation time, the concentrations of metal ions and reducing agents, and the temperature. These conditions will need to be addressed in each experiment by optimizing the time and rate of amplification and by using proper controls. For silver staining of histopathology slices, we optimized these conditions,[41] and we recognize that the chemical conditions for optimal staining will vary from tissue to tissue.

The second challenge is the problem of multiplexing. Although multiplexed dark-field microscopy has been demonstrated using multiple nanoparticles with different sizes and compositions, this approach is challenging when combined with *in situ* growth of nanoparticles, because the growth of nanoparticles would need to be quenched to allow a different set of nanoparticles to be amplified. However, we have shown that these probes can be used simultaneously with a panel of fluorophores for multiplex imaging. The use of different optical imaging modalities increases multiplexing capabilities. These plasmonic nanoparticle scattering probes could be used for the detection of rare and low-abundance targets within the same sample, while fluorophores are used for more abundant targets, providing the multiplexing capabilities required for analysis of multiple molecules within the tissue. We have shown that the fluorescence and scattering signals can be separated using their distinct spectral profiles even when they are excited by the same laser source, making this an ideal combined imaging approach. Additionally, we have shown that a variety of nanomaterials are compatible with *in situ* metal deposition. This now allows researchers to compare the spatial distributions of upconverting nanoparticles, persistent-luminescence nanoparticles, quantum dots, and other nonfluorescent probes in transparent tissues.[42,43]

Another avenue for multiplexed imaging using optical scattering labels could be achieved using hyperspectral dark-field microscopy applied to 3D whole-organ imaging. This is required because although spectrally distinct scattering probes can be prepared, they often produce overlapping signals that

DOI: 10.1021/jacs.7b04022
J. Am. Chem. Soc. 2017, 139, 9961−9971

can only be decoupled by examining the whole spectrum. The next step requires the development of a specialized lightsheet microscope that can illuminate with a plane of white light. The addition of spectral decoupling to the high imaging speed of lightsheet microscopy will allow the acquisition of a nearly unlimited number of scattering and fluorescent signals, making it possible to examine both the expression profiles and structural context of cells in whole tissues simultaneously. Nevertheless, the development and assessment of new chemical probes, microscopy techniques, and algorithms are required to ensure that these techniques will be central tools for studying disease pathophysiology and progression.

MATERIALS AND METHODS

All of the animals were fixed and gelled using 4% paraformaldehyde, 2% acrylamide, 1× PBS, and 0.25% Va-044 initiator and cleared using 4% SDS at 50 °C for 7−14 days. AuNPs used for injection were synthesized according to the Frens method for nanoparticles up to 15 nm in diameter and the Perrault method for larger nanoparticles. For injection into animals, nanoparticles were PEGylated using HS-PEG(5 kDa)-OMe. For molecular labeling, AuNPs were conjugated with GSL1-Cy5 using the heterobifunctional OPSS-PEG-NHS cross-linker at a 150:1 ratio of protein to AuNP and backfilled with HS-PEG(2 kDa)-OMe. Gold and silver enhancement was achieved by sequentially incubating cleared tissues in 0.1% TritonX-100 in 200 mM borate buffer for 1 day, gold or silver solution in deionized water for 4 h to 2 days, 0.1% TritonX-100 in 200 mM borate buffer for 1 h, and 67% 2,2′-thiodiethanol for 1 day. Full details are available in the Supporting Information.

ASSOCIATED CONTENT

Supporting Information

The Supporting Information is available free of charge on the ACS Publications website at DOI: 10.1021/jacs.7b04022.

Detailed methods, nanoparticle and imaging characterization, further details of *in situ* gold deposition and molecular labeling, and descriptions of the videos (PDF)

3D visualization of AuNPs in kidney tissue (AVI)

3D visualization of AuNPs in intestinal tissue (AVI)

3D visualization of tumor tissue containing AuNPs without amplification (AVI)

3D visualization of tumor tissue containing AuNPs after amplification (AVI)

3D visualization of spinal cord tissue of healthy mice (AVI)

3D visualization of labeled lesions in spinal cord tissue of a mouse model of multiple sclerosis (AVI)

AUTHOR INFORMATION

Corresponding Author

*warren.chan@utoronto.ca

ORCID

Stefan Wilhelm: 0000-0003-2167-6221

Warren C. W. Chan: 0000-0001-5435-4785

Author Contributions

#A.M.S. and S.S. contributed equally to this work.

Notes

The authors declare no competing financial interest.

ACKNOWLEDGMENTS

We acknowledge Doug Holmyard of the Nanoscale Bioimaging Facility at the Hospital for Sick Children, Toronto, for preparing the tissue slices for TEM and Dr. Neil Coombs from the Centre for Nanostructure Imaging (University of Toronto) for his assistance with SEM and EDX analysis. We also acknowledge the Canadian Institutes of Health Research (CIHR) and the Natural Sciences and Engineering Research Council (NSERC) for supporting the project. S.S. and A.M.S. acknowledge CIHR and NSERC, respectively, for student fellowships. B.K. acknowledges the Wildcat Fellows Program for his student fellowship.

REFERENCES

(1) Underwood, J. C. *Histopathology* **2017**, *70*, 4.

(2) Shaner, N. C.; Steinbach, P. A.; Tsien, R. Y. *Nat. Methods* **2005**, *2*, 905.

(3) Resch-Genger, U.; Grabolle, M.; Cavaliere-Jaricot, S.; Nitschke, R.; Nann, T. *Nat. Methods* **2008**, *5*, 763.

(4) Keller, P. J.; Dodt, H. U. *Curr. Opin. Neurobiol.* **2012**, *22*, 138.

(5) Becker, K.; Jahrling, N.; Kramer, E. R.; Schnorrer, F.; Dodt, H. U. *J. Biophotonics* **2008**, *1*, 36.

(6) Dodt, H. U.; Leischner, U.; Schierloh, A.; Jahrling, N.; Mauch, C. P.; Deininger, K.; Deussing, J. M.; Eder, M.; Zieglgansberger, W.; Becker, K. *Nat. Methods* **2007**, *4*, 331.

(7) Tainaka, K.; Kubota, S. I.; Suyama, T. Q.; Susaki, E. A.; Perrin, D.; Ukai-Tadenuma, M.; Ukai, H.; Ueda, H. R. *Cell* **2014**, *159*, 911.

(8) Chung, K.; Deisseroth, K. *Nat. Methods* **2013**, *10*, 508.

(9) Belle, M.; Godefroy, D.; Couly, G.; Malone, S. A.; Collier, F.; Giacobini, P.; Chedotal, A. *Cell* **2017**, *169*, 161.

(10) Eggeling, C.; Widengren, J.; Rigler, R.; Seidel, C. A. *Anal. Chem.* **1998**, *70*, 2651.

(11) Lee, D.-E.; Koo, H.; Sun, I.-C.; Ryu, J. H.; Kim, K.; Kwon, I. C. *Chem. Soc. Rev.* **2012**, *41* (7), 2656.

(12) Jain, P. K.; Lee, K. S.; El-Sayed, I. H.; El-Sayed, M. A. *J. Phys. Chem. B* **2006**, *110*, 7238.

(13) Cui, Y.; Wang, X. L.; Ren, W.; Liu, J.; Irudayaraj, J. *ACS Nano* **2016**, *10*, 3132.

(14) England, C. G.; Huang, J. S.; James, K. T.; Zhang, G. D.; Gobin, A. M.; Frieboes, H. B. *PLoS One* **2015**, *10*, e0129172.

(15) Bickford, L. R.; Agollah, G.; Drezek, R.; Yu, T. K. *Breast Cancer Res. Treat.* **2010**, *120*, 547.

(16) Sindhwani, S.; Syed, A. M.; Wilhelm, S.; Glancy, D. R.; Chen, Y. Y.; Dobosz, M.; Chan, W. C. W. *ACS Nano* **2016**, *10*, 5468.

(17) Sindhwani, S.; Syed, A. M.; Wilhelm, S.; Chan, W. C. W. *Bioconjugate Chem.* **2017**, *28*, 253.

(18) Tomer, R.; Ye, L.; Hsueh, B.; Deisseroth, K. *Nat. Protoc.* **2014**, *9*, 1682.

(19) Renier, N.; Wu, Z. H.; Simon, D. J.; Yang, J.; Ariel, P.; Tessier-Lavigne, M. *Cell* **2014**, *159*, 896.

(20) Murray, E.; Cho, J. H.; Goodwin, D.; Ku, T.; Swaney, J.; Kim, S. Y.; Choi, H.; Park, Y. G.; Park, J. Y.; Hubbert, A.; Mccue, M.; Vassallo, S.; Bakh, N.; Frosch, M. P.; Wedeen, V. J.; Seung, H. S.; Chung, K. *Cell* **2015**, *163*, 1500.

(21) Liebmann, T.; Renier, N.; Bettayeb, K.; Greengard, P.; Tessier-Lavigne, M.; Flajolet, M. *Cell Rep.* **2016**, *16*, 1138.

(22) Turkevich, J.; Stevenson, P. C.; Hillier, J. *Discuss. Faraday Soc.* **1951**, *11*, 55.

(23) Perrault, S. D.; Chan, W. C. W. *J. Am. Chem. Soc.* **2009**, *131*, 17042.

(24) Gage, S. H. *Trans. Am. Microsc. Soc.* **1920**, *39*, 95.

(25) Mertz, J.; Kim, J. *J. Biomed. Opt.* **2010**, *15*, 016027.

(26) Babar, S.; Weaver, J. H. *Appl. Opt.* **2015**, *54*, 477.

(27) Mondin, G.; Wisser, F. M.; Leifert, A.; Mohamed-Noriega, N.; Grothe, J.; Dörfler, S.; Kaskel, S. *J. Colloid Interface Sci.* **2013**, *411*, 187.

(28) Duan, C.; Adam, V.; Byrdin, M.; Ridard, J.; Kieffer-Jaquinod, S.; Morlot, C.; Arcizet, D.; Demachy, I.; Bourgeois, D. *J. Am. Chem. Soc.* **2013**, *135*, 15841.

(29) Song, L. L.; Varma, C. A. G. O.; Verhoeven, J. W.; Tanke, H. J. *Biophys. J.* **1996**, *70*, 2959.

(30) Wray, W.; Boulikas, T.; Wray, V. P.; Hancock, R. *Anal. Biochem.* **1981**, *118*, 197.

DOI: 10.1021/jacs.7b04022
J. Am. Chem. Soc. 2017, 139, 9961−9971

(31) Laitinen, L. *Histochem. J.* **1987**, *19*, 225.
(32) Dai, Q.; Walkey, C.; Chan, W. C. W. *Angew. Chem., Int. Ed.* **2014**, *53*, 5093.
(33) Loo, C.; Lin, A.; Hirsch, L.; Lee, M.-H.; Barton, J.; Halas, N.; West, J.; Drezek, R. *Technol. Cancer Res. Treat.* **2004**, *3*, 33.
(34) Wilhelm, S.; Tavares, A. J.; Dai, Q.; Ohta, S.; Audet, J.; Dvorak, H. F.; Chan, W. C. W. *Nat. Rev. Mater.* **2016**, *1*, 16014.
(35) Legroux, L.; Pittet, C. L.; Beauseigle, D.; Deblois, G.; Prat, A.; Arbour, N. *J. Neurosci. Methods* **2015**, *247*, 23.
(36) Recks, M. S.; Addicks, K.; Kuerten, S. *Neurosci. Lett.* **2011**, *494*, 227.
(37) Constantinescu, C. S.; Farooqi, N.; O'Brien, K.; Gran, B. *Br. J. Pharmacol.* **2011**, *164*, 1079.
(38) Li, W.; Chen, X. *Nanomedicine (London, U. K.)* **2015**, *10*, 299.
(39) Wang, L. V.; Yao, J. *Nat. Methods* **2016**, *13* (8), 627.
(40) Kircher, M. F.; de la Zerda, A.; Jokerst, J. V.; Zavaleta, C. L.; Kempen, P. J.; Mittra, E.; Pitter, K.; Huang, R.; Campos, C.; Habte, F.; Sinclair, R.; Brennan, C. W.; Mellinghoff, I. K.; Holland, E. C.; Gambhir, S. S. *Nat. Med.* **2012**, *18* (5), 829.
(41) Chou, L. Y. T.; Fischer, H. C.; Perrault, S. D.; Chan, W. C. W. *Anal. Chem.* **2009**, *81* (11), 4560.
(42) Li, Z. J.; Zhang, Y. W.; Wu, X.; Huang, L.; Li, D. S.; Fan, W.; Han, G. *J. Am. Chem. Soc.* **2015**, *137*, 5304.
(43) Wu, X.; Zhang, Y. W.; Takle, K.; Bilsel, O.; Li, Z. J.; Lee, H.; Zhang, Z. J.; Li, D. S.; Fan, W.; Duan, C. Y.; Chan, E. M.; Lois, C.; Xiang, Y.; Han, G. *ACS Nano* **2016**, *10*, 1060.

DOI: 10.1021/jacs.7b04022
J. Am. Chem. Soc. 2017, 139, 9961−9971